Marín-Suárez, Marco; Peltonen, Joonas T.; Golubev, Dmitry S.; Pekola, Jukka P.

An electron turnstile for frequency-to-power conversion

Published in:
Nature Nanotechnology

DOI:
10.1038/s41565-021-01053-5

Published: 01/03/2022

Document Version
Peer-reviewed accepted author manuscript, also known as Final accepted manuscript or Post-print

Please cite the original version:
Marín-Suárez, M., Peltonen, J. T., Golubev, D. S., & Pekola, J. P. (2022). An electron turnstile for frequency-to-power conversion. *Nature Nanotechnology*, *17*(3), 239-243. https://doi.org/10.1038/s41565-021-01053-5

An electron turnstile for frequency to power conversion

Marco Marín-Suárez,[1,*] Joonas T. Peltonen,[1] Dmitry S. Golubev,[1] and Jukka P. Pekola[1,2]

[1] *Pico group, QTF Centre of Excellence, Department of Applied Physics, Aalto University, FI-000 76 Aalto, Finland*
[2] *Moscow Institute of Physics and Technology, 141700 Dolgoprudny, Russia*

Single-electron transport relates an operation frequency f to the emitted current I through the electron charge e as $I = ef$ [1–5]. Similarly, direct frequency to power conversion (FPC) links both quantities through a known energy. FPC is a natural candidate for a power standard resorting to the most basic definition of the watt: energy emitted per unit of time. The energy is traceable to Planck's constant h, the time is in turn traceable to the unperturbed ground state hyperfine transition frequency of the caesium 133 atom $\Delta\nu_{\mathrm{Cs}}$. Hence, FPC comprises a simple and elegant way to realize the watt [6]. In this spirit, single-photon emission [7, 8] and detection [9] at known rates have been proposed as radiometric standard and experimentally realized [10–14]. However, power standards are so far only traceable to electrical units, i.e., to volt and ohm [6, 15–17]. In this letter, we demonstrate an alternative proposal based on solid-state direct FPC using a SINIS (S = superconductor, N = normal metal, I = insulator) single-electron transistor (SET). The SET injects n (integer) quasi-particles per cycle to the two superconducting leads with discrete energies close to their superconducting gap Δ, even at zero source-drain voltage. Furthermore, the application of a bias voltage can vary the distribution of the power among the two leads, allowing for an almost equal power injection $n\Delta f$ to the two. While in single-electron transport current is related to a fixed universal constant (e), in our approach Δ is a material dependent quantity. We estimate that under optimized conditions errors can be well below 1%.

The FPC process can be understood based on a simplified picture of a driven NIS junction (Fig. 1a) by looking at the quasi-particle (qp) injection dynamics. The key property here is the singularity of the superconducting density of states at energies $\pm\Delta$ as counted from the Fermi level. During the periodic driving the chemical potential of the normal island is shifted by an applied gate voltage V_{g}, and at certain time an electron tunnels into the superconductor with energy close to Δ. Later on, the driving provides enough energy for an electron to tunnel into the island breaking a Cooper pair and leaving an excitation in the superconductor, again close to the gap-edge. Thus, two tunnelling events per cycle occur. For larger driving amplitudes $2n$ tunnelling events are allowed. Within this picture, in a SINIS structure the tunnelling events at bias voltage $V_{\mathrm{b}} = 0$ occur stochastically through both junctions with probabilities proportional to their transparencies. This results in a total energy injection of $2n\Delta$ per cycle in the absence of net electric, and consequently, particle current. At sufficiently large non-zero bias a preferred direction for the charge transfer appears and in every cycle n tunnelling events occur in each junction regardless of their transparencies, as depicted in Fig. 1b. Therefore, the total injected energy is almost equally split between the two leads, but remains nearly unchanged compared to zero bias case. Thus, the time averaged power generated by an ideal FPC converter equals to

$$P = 2n\Delta f, \tag{1}$$

and would exhibit a structure of plateaus similar to the charge current pumped through SINIS turnstiles [3], but now even at zero bias voltage. Accuracy of Eq. (1) can be tested in the FPC device depicted in Fig. 1c (see Supplementary Section S1 for its characterization).

This device constitutes a turnstile for single electrons (see Supplementary Figure S1) when the island (light red short structure in Figure 1c) is periodically driven at frequency f with a radio-frequency (rf) signal applied to a capacitively coupled, via the capacitance C_{g}, gate electrode. At proper source-drain biases and driving amplitudes, an average charge current $I = nef$ flows through both tunnel-contacted leads (light blue short structure in Fig. 1c) as a consequence of the dynamics described in Fig. 1b. The injected qps transport energy approximately without losses across the narrow leads [18, 19] to directly interfaced normal-metal traps (light red long structures). These structures act as bolometers for measuring quantitatively the heat generated by the qp injection, accounting completely for the power [20]. The conventional normal-metal electron-phonon interaction model [21] accounts for this heat via $P = \Sigma\mathcal{V}\left(T_{\mathrm{e}}^5 - T_{\mathrm{b}}^5\right)$. Here Σ is the electron-phonon coupling constant of the material, $\mathcal{V}$ the trap volume, T_{e} its electron temperature and T_{b} the phonon bath temperature which usually can be taken as the cryostat temperature [22]. The bolometer $\Sigma\mathcal{V}$ factor is calibrated *in-situ* here with an uncertainty $\sim 10\%$. See Supplementary Section S2 for details on the calibration of this detector. Current-biased superconducting tunnel probes (vertical blue structures in Fig. 1c) contacted to the trap help determining T_{e} by measuring the corresponding voltage drop (see Supplementary Section S3 for the temperature calibration of these thermometers). The measured power can be compared to the

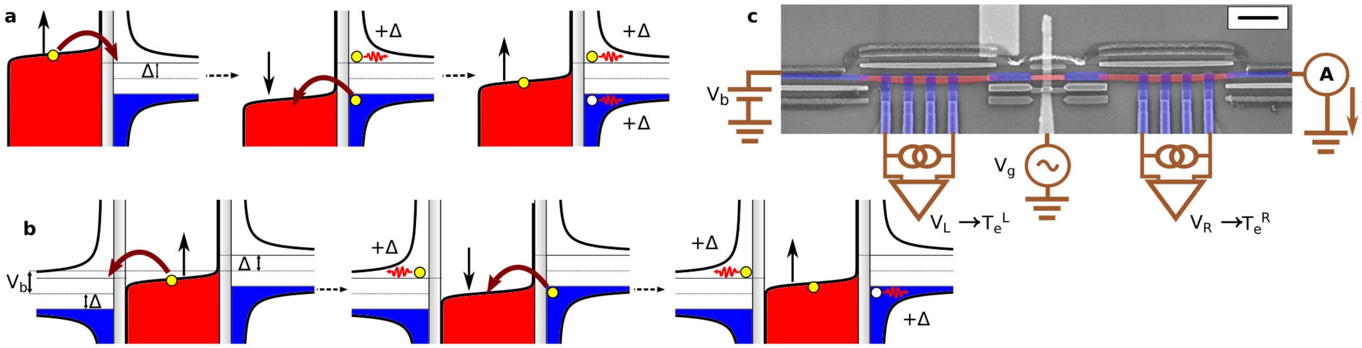

FIG. 1. **Single-electron turnstile for Frequency to Power Conversion.** (a) Sketch illustrating the operation at zero bias exemplified in a hybrid single-electron box. The chemical potential of the normal electrode (left) is varied periodically. First, an electron (yellow dot) has enough energy to be injected into the superconducting lead (right) at the gap edge from the island as an excitation. Later, the driving enables an electron to tunnel from the lead to the island while the previously injected excitation diffuses. Once this electron tunnels to the island, it leaves one excited state close to the gap edge in the lead. Total energy of twice the superconducting gap (2Δ) is injected into the lead per cycle. In the case of a turnstile at zero bias, the operation is the same as here, but the tunnelling events occur stochastically through the two contacts. (b) Sketch illustrating the non-zero bias behaviour in FPC. As opposed to the zero bias case, the excitations are created in both leads, giving again a total injected energy of 2Δ per cycle distributed equally to the two leads. (c) Coloured scanning electron micrograph. Light red refers to normal-metal and blue to superconductor. Scale bar is $1\,\mu$m. We show the experimental setup for measuring the injected power in the turnstile operation. V_{b}, bias voltage; V_{g}, gate voltage; I, emitted current; V_{L} and V_{R}, voltage measured in the the left and right bolometer, respectively; $T_{\mathrm{e}}^{\mathrm{L}}$ and $T_{\mathrm{e}}^{\mathrm{R}}$, transduced electronic temperatures from the corresponding measured voltages.

expected FPC outcome.

Fig. 2 presents the total injected power $P_{\mathrm{T}} = P_{\mathrm{R}} + P_{\mathrm{L}}$, the main result of this work, here $P_{\mathrm{L(R)}}$ is the power measured by the left (right) bolometer. We applied a gate signal $V_{\mathrm{g}} = V_{0\mathrm{g}} + A_{\mathrm{g}} \sin(2\pi f t)$ with $f = 80\,\mathrm{MHz}$ and swept $V_{0\mathrm{g}}$ over various gate periods keeping $V_{\mathrm{b}} = 0$. Simultaneously, we vary A_{g} so that the gate-induced charge spans several charge stability regions in the Coulomb diamonds of the SET. Power plotted versus $V_{0\mathrm{g}}$ and A_{g} exhibits plateaus of (approximately) constant value, closely following Eq. (1) and confirming the dynamics described in Figs. 1a and 1b. It also reveals the e-periodic nature of the injected energy in the DC gate voltage. Thus, we confirm that excitations are created close to the superconductor gap edge. The similarity of the plateaux pattern with that of Figure 2a in Ref. 3 is evident and shows parallelism between the frequency to current conversion of single-electron transport and our proposal of frequency to power conversion, with FPC being possible even at zero bias $V_{\mathrm{b}} = 0$.

Fig. 3 presents further measurements of the power production at zero bias. Panel 3a shows the total injected power for $C_{\mathrm{g}}V_{0\mathrm{g}}/e = 0.5$ and a wide range of driving frequencies confirming the results of Fig. 2 at different injected powers. Panel b shows that the total generated energy is close to ideal FPC. Indeed, the conversion errors range from 1.51% to 6.32% at low frequency $f = 20\,\mathrm{MHz}$ and from 4.48% to 14.26% at higher frequency $f = 160\,\mathrm{MHz}$. Calculations (solid lines) of the generated power resulting from a Markovian model (used also for DC characterization, See Supplementary Section S4) can reproduce the gate amplitude and frequency dependencies. Panels c and d exhibit the individual contributions to the power in the left and right lead, respectively. Notice that the two are not equal as explained above.

We gain more insight into the dynamics of the zero bias operation by simulating the instantaneous behaviour of the device. Figure 3e shows the calculated time dependent total injected power (Eq. (5), red curve) and current through one junction (Eq. (4), blue curve) as function of the electrostatic energy change during an electron tunnelling event into the island $\varepsilon(t) = 2E_{\mathrm{c}}(0.5 - n_{\mathrm{g}}) = -(2E_{\mathrm{c}}A_{\mathrm{g}}C_{\mathrm{g}}/e)\sin(2\pi f t)$ for $n_{\mathrm{g}} = C_{\mathrm{g}}V_{\mathrm{g}}/e$, $C_{\mathrm{g}}V_{0\mathrm{g}}/e = 0.5$ and $V_{\mathrm{b}} = 0$. Here E_{c} is the system charging energy. The inset of Figure 3e shows the evolution of ε for a driving with amplitude at the start of the first plateau and period τ. It is clear that only electrons within a narrow energy band around Δ tunnel in and out of the island through the same junction thus cancelling the current and supporting Eq. (1). The tunnelling events happen in both junctions with relative probabilities inversely proportional to their resistances.

We show in Fig. 3f that a device with proper E_{c}, total normal-state resistance R_{T} and Dynes parameter [23] η can provide better FPC accuracy. We used $E_{\mathrm{c}} = \Delta = 200\,\mu\mathrm{eV}$, $R_{\mathrm{T}} = 200\,\mathrm{k\Omega}$ and $\eta = 10^{-6}$ for calculating the total injected power solving the same Markovian model used. We assume low but achievable temperatures ($T_{\mathrm{S}}^{\mathrm{L}} = T_{\mathrm{S}}^{\mathrm{R}} = 150\,\mathrm{mK}$, $T_{\mathrm{N}} = 10\,\mathrm{mK}$, for left and right lead and island, respectively). When the driving is slow ($f = 1\,\mathrm{MHz}$) the accuracy of the injected power

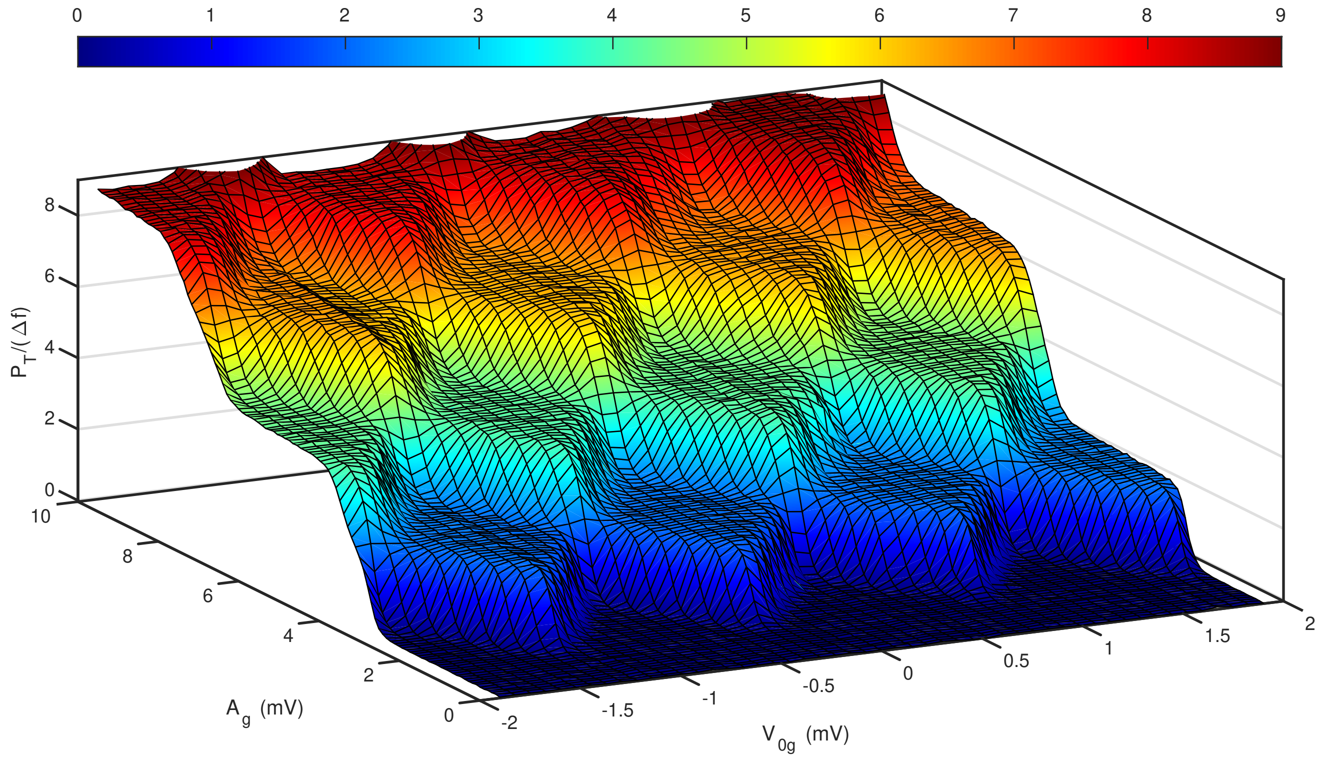

FIG. 2. **Power injection at zero bias.** Total injected power at $f = 80\,\mathrm{MHz}$ and $V_\mathrm{b} = 0$ measured at $T_\mathrm{b} = 130\,\mathrm{mK}$ as a function of the gate offset $V_{0\mathrm{g}}$ spanning several periods. The power is ideally given by $P = 2n\Delta f$ with n an integer. Here the gate amplitude A_g range is such that four pumping plateaus become visible. It is evident that the injected power follows the diamond pattern, here even in the absence of average current through the device. Colorbar scale is the same as z-axis scale.

is within 0.20% and 0.65% in the first plateau and it varies between 1.27% and 3.8% for $f = 80\,\mathrm{MHz}$. Thus it is possible, in principle, to achieve accurate power injection of $2\Delta f$ provided that η is sufficiently small and temperatures are low. The capability of measuring small powers bolometrically sets the ultimate limitation of accuracy under these conditions: at 1 MHz the power is $\sim 0.3\,\mathrm{fW}$ which exceeds the noise level in a standard setup by two orders of magnitude [24]. The bolometer noise is dominant over the shot noise of the generated energy flux caused by the stochastic nature of electron tunnelling, see Supplementary Section S5. Yet at these operation frequencies the Dynes parameter starts to play an important role making the power lower than Eq. (1) predicts. Additionally, we have verified that injection errors scale as $\propto \left(E_\mathrm{c} e^2 R_\mathrm{T} f/\Delta^2\right)^{2/3}$, thus higher power emission with better accuracy is possible for more transparent junctions. Yet in this argument we ignore the influence of Andreev tunnelling power injection [25].

The Markovian model straightforwardly shows how the power is distributed to the two leads (see details in Supplementary Section S6). The absence of a preferred direction of flow (i.e., zero bias voltage) together with assuming the same qp temperature for both leads yield

$$\frac{P_\mathrm{R}}{P_\mathrm{L}} = \frac{R_\mathrm{L}}{R_\mathrm{R}}. \tag{2}$$

Here $R_{\mathrm{L(R)}}$ is the normal-state left (right) junction resistance. For the present device, we determined by the DC characterization $R_\mathrm{L}/R_\mathrm{R} = 0.65$. The ratios shown in Figs. 3g (calculated from data of Fig. 2) and 3h (from data in Figs. 3c and 3d) match this value, validating Eq. (2). Thus, the power is distributed according to the ratio of junction transparencies irrespective of the gate voltage and temperature.

Figs. 4a and 4b illustrate two representative cases of FPC operation at non-zero bias (see Extended Data Figs. 1–3 for additional data). In Fig. 4a we present the data for $f = 20\,\mathrm{MHz}$ and $V_\mathrm{b} = 240\,\mu\mathrm{V}$. The device pumps a single-electron current close to the expected value ef, and its behaviour is well described by our simulations, see the inset. We find that the total generated power closely follows Eq. (1) also in this case. The main difference in comparison to the unbiased device concerns the distribution of power between the left and the right leads. Large bias voltage sets the preferred direction of tunnelling for electrons and, therefore, makes the number of electrons transferred through the two tunnel junctions equal. Consequently, the injected power splits almost

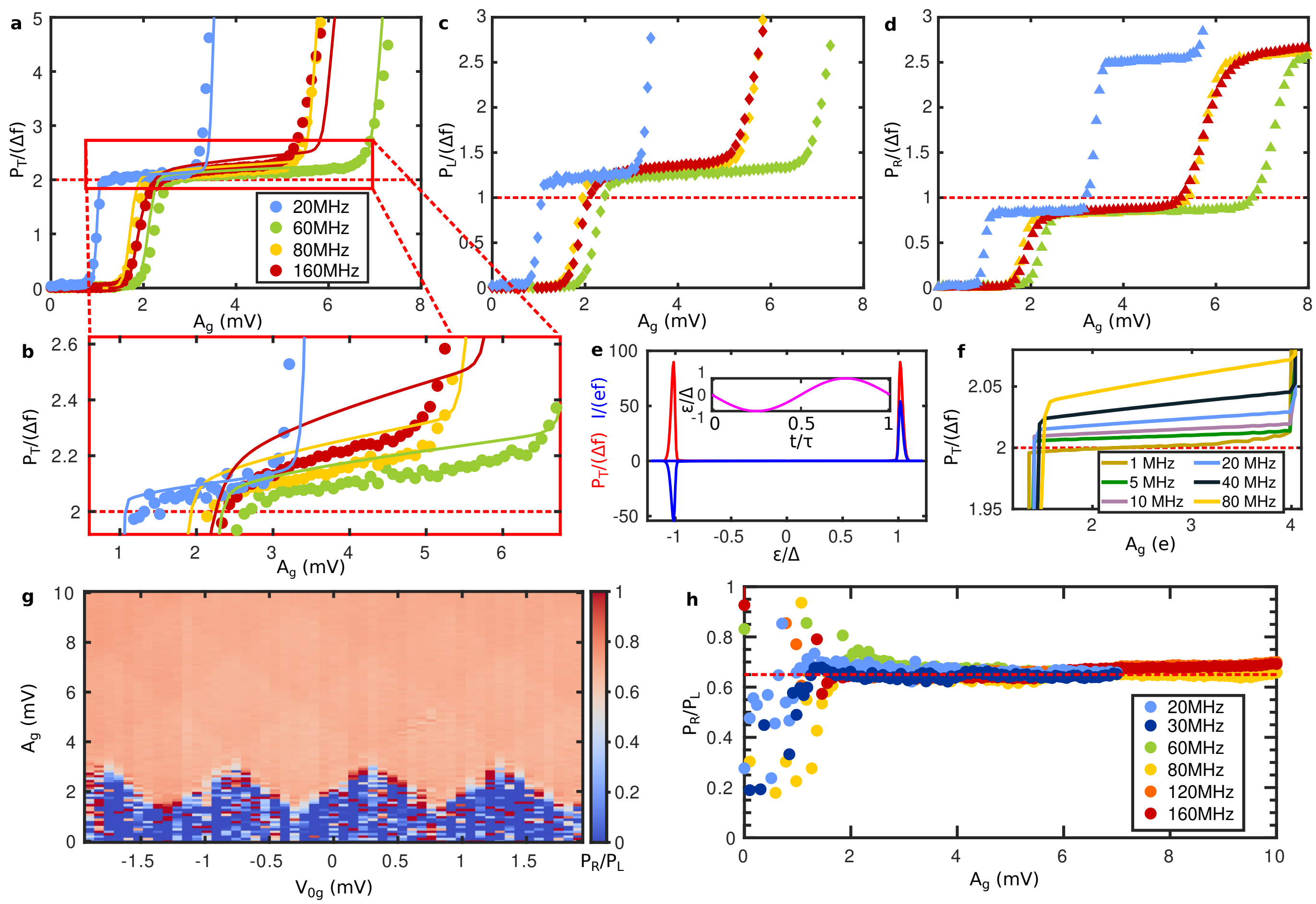

FIG. 3. **Power injection and dynamical behaviour of the device at zero bias.** (a) Power injected to the two leads in the absence of average current ($V_\mathrm{b} = 0$) with $C_\mathrm{g}V_{0\mathrm{g}}/e = 0.5$, a power $\sim 2\Delta f$ is generated in the first plateau at different driving frequencies. Solid lines are calculated and dots are data measured at $T_\mathrm{b} = 117\,\mathrm{mK}$. (b) Close-up of panel (a) to the first power plateau, the calculated curves follow the trend of the data. (c) Power injected into the right lead and (d) into the left lead. Notice that, transmission of the rf gate voltage depends on frequency giving different A_g dependences of the otherwise similar power plateaux for different frequencies. (e) Simulation of instantaneous total injected power (red line) and current (blue line) as a function of the chemical potential difference for a jump into the island. The inset shows the evolution of this energy within one driving period. Here, the measured device parameters are used and $f = 5\,\mathrm{MHz}$, $T_\mathrm{S}^\mathrm{L} = T_\mathrm{S}^\mathrm{R} = T_\mathrm{N} = 10\,\mathrm{mK}$. (f) Total injected power plateaus calculated for a turnstile with more optimized, but realistic, parameters (see the text) and triangular gate driving. (g) and (h) Measured ratio between the injected power in the right and left leads as a function of the gate offset, amplitude and frequency. For (g) data are from Fig. 2, whereas for (h) data are from panels (c) and (d). Notice that this ratio is insensitive to the varied parameters and equal to the inverse of the normal-state junction resistance ratio.

equally between the two leads. Looking more closely, we find that both in the experiment and in the simulations P_R slightly exceeds P_L, i.e., the distribution of the powers is inverted with respect to zero bias case. This can be understood as follows: more energy needs to be provided for tunnelling through the more resistive junction, which is bound to happen before a tunnelling event can occur through the more transparent junction since driving is slower than the tunnelling rates. In this case, the power peaks of Fig. 3e move further into the region $|\varepsilon| > \Delta$.

In Fig. 4b we present the data measured at higher frequency $f = 60\,\mathrm{MHz}$ and at $V_\mathrm{b} = 160\,\mu\mathrm{V}$. We find that at high gate modulation amplitudes a small current opposite to the bias begins to flow. This behaviour is well captured by our simulations. We observe that $P_\mathrm{R} > P_\mathrm{L}$ for gate amplitudes close to the onset of the current plateau similarly to Fig. 4a. At higher modulation amplitudes, where tunnelling against the bias (back-tunnelling) is energetically possible, we find $P_\mathrm{R} < P_\mathrm{L}$ similarly to zero bias case. In this regime, two tunnelling events during one cycle more frequently occur in the less resistive junction and, therefore, inject more energy to the left lead. The ratio $P_\mathrm{R}/P_\mathrm{L}$ decreases with the modulation amplitude, but it remains above its zero bias value, $P_\mathrm{R}/P_\mathrm{L} \geq R_\mathrm{L}/R_\mathrm{R}$. Notice that back-tunnelling is energetically possible in the two previous situations but happens

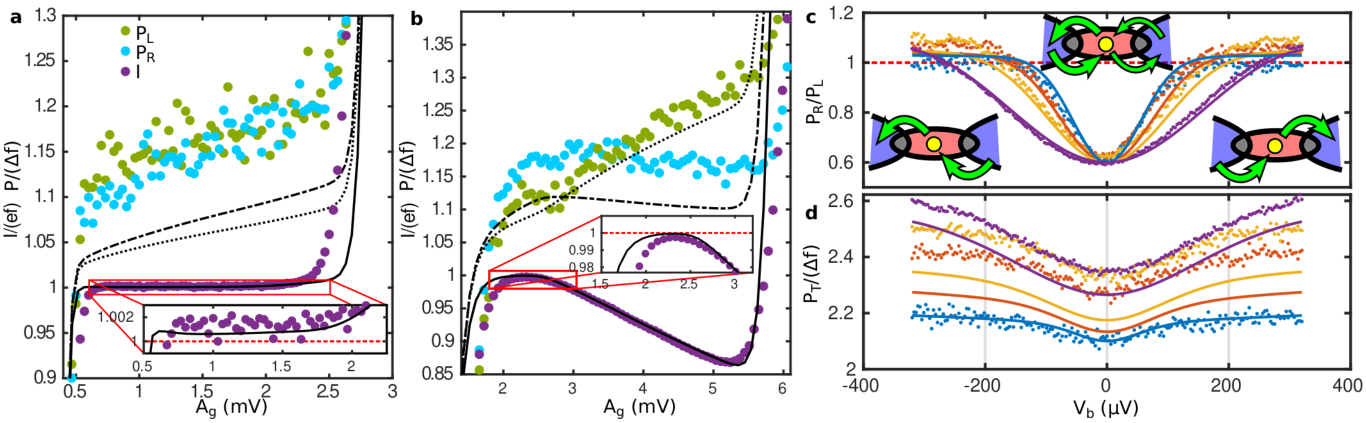

FIG. 4. **Power injection at non-zero bias.** Data measured at $T_\mathrm{b} = 117\,\mathrm{mK}$ (a) Charge current (purple filled circles) and injected power to the left (green circles) and right (cyan circles) traps at $V_\mathrm{b} = 240\,\mu\mathrm{V}$ and $f = 20\,\mathrm{MHz}$ against the gate amplitude. Black lines are simulations of charge current (solid), power injected into the left (dotted) and right (dash-dotted) leads, from the Markovian model. In this situation, the power is almost equally distributed to both leads. (b) As in (a) for $V_\mathrm{b} = 160\,\mu\mathrm{V}$ and $f = 60\,\mathrm{MHz}$, here the driving rate is comparable to the tunnelling rates. As a consequence the current and power injected to the right lead plateaus bend down and therefore the less transparent junction transmits less power. (c) Measured (dots) and calculated (solid lines) injected power ratios on the first plateau for driving frequencies $f = 30$, 60, 80, 160 MHz in blue, red, yellow and purple, respectively, as function of the bias. Two observations can be made, the ratio approaches 1 (i.e., one tunnelling event occurs per junction unidirectionally, see the cartoons) as the absolute value of bias increases and it converges to $R_\mathrm{L}/R_\mathrm{R}$ at $V_\mathrm{b} = 0$ for all the frequencies. (d) As in (c) for the total heat injected. The heat deviates from the value $P = 2\Delta f$ when the driving frequency becomes comparable to the tunnelling rates.

only when $\dot{\varepsilon}$ is comparable to tunnelling rates at $\varepsilon \gtrsim \Delta$ as is the case for $f = 60\,\mathrm{MHz}$.

In Fig. 4c we show the ratio $P_\mathrm{R}/P_\mathrm{L}$ at the plateau as a function of the bias voltage for several frequencies. As expected, at $V_\mathrm{b} = 0$ we obtain $P_\mathrm{R}/P_\mathrm{L} = R_\mathrm{L}/R_\mathrm{R}$ for all frequencies. Cartoons in Fig. 4c and Extended Data Fig. 4 illustrate the tunnelling processes relevant to the corresponding bias regimes. At $f = 30\,\mathrm{MHz}$ (blue dots), i.e. at slow driving where back-tunnelling can be ignored, we observe $P_\mathrm{R}/P_\mathrm{L} \approx 1$ already at low bias. Because of the back-tunnelling at higher driving frequencies stronger bias is required to bring the ratio close to 1 (visible also in Extended Data Figs. 2 and 3). At frequencies comparable to the tunnelling rates the distribution of the tunnelled energies ε becomes wide and for this reason the average energy emitted during a single tunnelling event grows, see Supplementary Section S7. We illustrate this point in Fig. 4d. In general, at lower frequencies the injected power is less sensitive to the bias voltage. All these effects are accurately captured by the Markovian model, the results of the corresponding simulations are shown by solid lines in Figs. 4c and 4d.

In summary, we have demonstrated synchronized and controlled power injection in periodically driven NIS junctions, which is well described by a stochastic Markovian model. We achieve high electron energy selectivity thanks to the singularity in the superconducting density of states. This energy is then measured by a normal metal bolometer trapping the excitations. The device generates a total power of $2n\Delta f$ due to the controlled qp injection rate. This allows measurement of a power as a known energy ($2n\Delta$) released at a given repetition rate (f) analogously to the single-electron transport *mise en pratique* of the ampere [6]. In contrast with single-photon sources, whose highest achieved emission efficiencies do not exceed 60% [14], our implementation is an on-demand precise energy source. The used SINIS geometry allows accurate *in situ* measurement of the superconducting gap by standard tunnel spectroscopy, as done here. While frequency to current conversion does not need independent determination of e (it is fixed by definition), FPC requires an independent measurement of Δ, which adds further uncertainty. We estimate an uncertainty $< 1\%$ to our gap measurement (see inset in Fig. S1a and discussion) which exceeds the one in the operation frequency. Injection accuracy increases at low frequencies, but the detection method sets a lower bound for the generated power. Further improvements can be achieved by optimizing driving waveforms, device parameters or environmental conditions. Additionally, FPC would be achievable by having a δ-like singular density of states in the leads therefore increasing energy selectivity. This can be achieved, for example, by replacing the superconductors by quantum dots of tunable energy levels [26] hence providing a knob for increasing the power yield. This would enhance FPC accuracy since the synchronization of tunnelling events is ensured by the Coulomb blockade. Finally, FPC might find applications in nanoscale thermodynamics as a heat pump with no net particle flow [27–30] as well as in studying the dynamics of superconducting excitations because of the improved control of our realization compared to recent demonstrations [31].

ACKNOWLEDGEMENTS

We acknowledge O. Maillet and E. T. Mannila for useful discussions. This research made use of Otaniemi Research Infrastructure for Micro and Nanotechnologies (OtaNano) and its Low Temperature Laboratory. All authors thank funding from Academy of Finland through grant 312057. M.M.-S. and J.P.P. acknowledge support from European Union's Horizon 2020 research and innovation programme under the European Research Council (ERC) programme (grant agreement 742559). J.P.P. acknowledges funding from Russian Science Foundation (grant No. 20-62-46026).

AUTHOR CONTRIBUTIONS

M.M.-S. made part of the fabrication, carried out the measurements, performed simulations and analysed the data with important input of J.P.P. and D.S.G. J.T.P. fabricated most part of the devices and prepared the measurement instruments. D.S.G. and J.P.P. estimated the heat losses along the system. The primal idea was conceived by M.M.-S. and J.P.P. The manuscript was prepared by M.M-S. with important input from J.P.P, J.T.P and D.S.G.

COMPETING INTERESTS

The authors declare no competing interests.

* marco.marinsuarez@aalto.fi

[1] Geerligs, L. J. *et al.* Frequency-locked turnstile device for single electrons. *Phys. Rev. Lett.* **64**, 2691–2694 (1990).

[2] Kouwenhoven, L. P., Johnson, A. T., van der Vaart, N. C., Harmans, C. J. P. M. & Foxon, C. T. Quantized current in a quantum-dot turnstile using oscillating tunnel barriers. *Phys. Rev. Lett.* **67**, 1626–1629 (1991).

[3] Pekola, J. P. *et al.* Hybrid single-electron transistor as a source of quantized electric current. *Nat. Phys.* **4**, 120 (2007).

[4] Pekola, J. P. *et al.* Single-electron current sources: Toward a refined definition of the ampere. *Rev. Mod. Phys.* **85**, 1421–1472 (2013).

[5] Kaestner, B. & Kashcheyevs, V. Non-adiabatic quantized charge pumping with tunable-barrier quantum dots: a review of current progress. *Rep. Prog. Phys.* **78**, 103901 (2015).

[6] BIPM. *Mise en pratique for the definition of the ampere and other electrical units in the SI*, chap. Appendix 2 (Bureau international des poids et mesures, 2019), ninth edn. URL `https://www.bipm.org/en/publications/mises-en-pratique`.

[7] Vaigu, A. *et al.* Experimental demonstration of a predictable single photon source with variable photon flux. *Metrologia* **54**, 218–223 (2017).

[8] Rodiek, B. *et al.* Experimental realization of an absolute single-photon source based on a single nitrogen vacancy center in a nanodiamond. *Optica* **4**, 71 (2017).

[9] Zhu, D. *et al.* Resolving photon numbers using a superconducting nanowire with impedance-matching taper. *Nano Lett.* **20**, 3858–3863 (2020).

[10] Zwinkels, J. C., Ikonen, E., Fox, N. P., Ulm, G. & Rastello, M. L. Photometry, radiometry and 'the candela': evolution in the classical and quantum world. *Metrologia* **47**, R15–R32 (2010).

[11] Chunnilall, C. J., Degiovanni, I. P., Kück, S., Müller, I. & Sinclair, A. G. Metrology of single-photon sources and detectors: a review. *Opt. Eng.* **53**, 081910 (2014).

[12] Lemieux, S., Giese, E., Fickler, R., Chekhova, M. V. & Boyd, R. W. A primary radiation standard based on quantum nonlinear optics. *Nat. Phys.* **15**, 529–532 (2019).

[13] Saha, S., Jaiswal, V. K., Sharma, P. & Aswal, D. K. Evolution of SI base unit candela: Quantifying the light perception of human eye. *MAPAN* **35**, 563–573 (2020).

[14] Tomm, N. *et al.* A bright and fast source of coherent single photons. *Nat. Nanotechnol.* **16**, 399–403 (2021).

[15] Palafox, L., Ramm, G., Behr, R., Ihlenfeld, W. K. & Moser, H. Primary AC power standard based on programmable josephson junction arrays. *IEEE Transactions on Instrumentation and Measurement* **56**, 534–537 (2007).

[16] Waltrip, B. *et al.* AC power standard using a programmable josephson voltage standard. *IEEE Transactions on Instrumentation and Measurement* **58**, 1041–1048 (2009).

[17] Waltrip, B. C., Nelson, T. L., Berilla, M., Flowers-Jacobs, N. E. & Dresselhaus, P. D. Comparison of AC power referenced to either PJVS or JAWS. *IEEE Transactions on Instrumentation and Measurement* **70**, 1–6 (2021).

[18] Peltonen, J. T. *et al.* Thermal conductance by the inverse proximity effect in a superconductor. *Phys. Rev. Lett.* **105**, 097004 (2010).

[19] Knowles, H. S., Maisi, V. F. & Pekola, J. P. Probing quasiparticle excitations in a hybrid single electron transistor. *Appl. Phys. Lett.* **100**, 262601 (2012).

[20] Ullom, J. N., Fisher, P. A. & Nahum, M. Measurements of quasiparticle thermalization in a normal metal. *Phys. Rev. B* **61**, 14839–14843 (2000).

[21] Giazotto, F., Heikkilä, T. T., Luukanen, A., Savin, A. M. & Pekola, J. P. Opportunities for mesoscopics in thermometry and refrigeration: Physics and applications. *Rev. Mod. Phys.* **78**, 217–274 (2006).

[22] Dorozhkin, S., Lell, F. & Schoepe, W. Energy relaxation of hot electrons and inelastic collision time in thin metal films at low temperatures. *Solid State Commun.* **60**, 245–248 (1986).

[23] Dynes, R. C., Narayanamurti, V. & Garno, J. P. Direct measurement of quasiparticle-lifetime broadening in a strong-coupled superconductor. *Phys. Rev. Lett.* **41**, 1509–1512 (1978).

[24] Ronzani, A. *et al.* Tunable photonic heat transport in a quantum heat valve. *Nat. Phys.* **14**, 991–995 (2018).

[25] Rajauria, S. *et al.* Andreev current-induced dissipation in a hybrid superconducting tunnel junction. *Phys. Rev.*

Lett. **100**, 207002 (2008).

[26] Prance, J. R. *et al.* Electronic refrigeration of a two-dimensional electron gas. *Phys. Rev. Lett.* **102**, 146602 (2009).

[27] Rey, M., Strass, M., Kohler, S., Hänggi, P. & Sols, F. Nonadiabatic electron heat pump. *Phys. Rev. B* **76**, 085337 (2007).

[28] Arrachea, L., Moskalets, M. & Martin-Moreno, L. Heat production and energy balance in nanoscale engines driven by time-dependent fields. *Phys. Rev. B* **75**, 245420 (2007).

[29] Kafanov, S. *et al.* Single-electronic radio-frequency refrigerator. *Phys. Rev. Lett.* **103**, 120801 (2009).

[30] Hussein, R., Kohler, S. & Sols, F. Heat pump driven by the shot noise of a tunnel contact. *Physica E* **77**, 156–163 (2016).

[31] Alegria, L. D. *et al.* High-energy quasiparticle injection into mesoscopic superconductors. *Nat. Nanotechnol.* **16**, 404–408 (2021).

METHODS

Fabrication

The samples were fabricated on 4-inch silicon substrates covered by 300 nm thermal silicon oxide. Masks were defined using electron beam lithography (EBL, Vistec EBPG500+ operating at 100 kV) and metallic layers deposited using multi-angle shadow evaporation in an electron-beam evaporator. Directly on top of the substrate, ground planes and gate electrodes were formed by deposition of a 2 nm titanium adhesion layer, 30 nm gold, and a further 2 nm Ti protection layer over a mask defined in a single layer positive resist (Allresist AR-P 6200). This initial deposition is covered, after lift-off, by a 50 nm insulating Al_2O_3 layer grown by atomic layer deposition (ALD). On top of this layer, a second EBL and metal evaporation process (2 nm Ti followed by 30 nm AuPd) is carried out to shape bonding pads and coarse electrodes connecting to the transistor leads and two tunnel probes, the rest of the bonding pads and electrodes are patterned in the third and final step. After a second lift-off process, NIS transistor and probe junctions, clean NS contacts and remaining bonding pads and electrodes are formed by EBL patterning on a Ge-based hard mask process [1, 4]. The mask is composed of a $\sim$ 400 nm P(MMA-MMA) copolymer layer, covered by 22 nm Ge also deposited by e-gun evaporation and a thin (approximately 50 nm) layer of PMMA on top. After cleaving the wafer into smaller chips (typically 1 cm $\times$ 1 cm), the pattern defined on the PMMA resist is transferred to the Ge layer by reactive ion etching (RIE) with CF_4. Next, an undercut profile is created in the copolymer layer by oxygen plasma in the same RIE. Creation of tunnel junctions is done first by evaporating a 30 nm layer of Al at a substrate tilt angle of -61.1°, resulting in a film that defines the finger-like superconducting probes. Right after deposition this layer is oxidized *in-situ* in the evaporator (static oxidation with typically 1.8 mbar for 1.5 minutes). A subsequent deposition of 30 nm Cu at approximately 39.1° tilt forms the normal-metal bolometers. Next, a second 30 nm layer of Al is evaporated at a tilt angle of -32.5° defining the transistor leads and the NS clean contacts. After a second oxidation (nominally 1.7 mbar O_2 for one minute), a final 40 nm Cu film was deposited at normal incidence forming the N island of the SINIS transistor. After a final conventional lift-off step, a chip with an array of 3×3 devices is cleaved to fit a custom-made chip carrier and electrically connected to it by Al wire bonds for measurements [2].

Measurements

A custom-made plastic dilution refrigerator with base temperature of about 100 mK was used to carry out measurements [2]. DC signals were applied through conventional cryogenic signal lines (resistive twisted pairs between room temperature and the 1 K flange, followed by at least 1 m Thermocoax cable as a microwave filter to the base temperature) connecting the bonded chip to a room temperature breakout box. Driving signals were transported to the gate by rf lines consisting of stainless steel coaxial cable down to 4.2 K, a 20 dB attenuator in the liquid helium bath, followed by a feedthrough into the inner vacuum can of the cryostat. Inside the cryostat, the rf signal is carried by a continuous superconducting NbTi coaxial cable from the 1 K stage down to the sample carrier. At room temperature, an additional 40 dB attenuation is applied to the signal. Signals were realized by programmable voltage sources and function generators. Voltage and current amplification was achieved by room temperature low-noise amplifier (FEMTO Messtechnik GmbH, model DLPVA-100-F-D) and transimpedance amplifier (FEMTO Messtechnik GmbH, model DDPCA-300), respectively. The bath temperature is controlled by applying voltage to a heating resistor attached to the sample holder. The curves of the pumped current were typically repeated at least 10 times and averaged accordingly, neglecting those repetitions during which a random offset charge jump had occurred. Current amplifier offset was subtracted by comparing the pumping curves with their counterparts measured under source-drain bias of opposite polarity. The voltage drop curves across both bolometers were also repeated at least 15 times and averaged the same way as the current. After calibrating the bolometers' response against a previously calibrated ruthenium oxide thermometer (Scientific Instruments, Inc., model RO-600) attached to the cryostat sample carrier holder, the electronic temperature of the normal-metal trap is obtained by a linear fit to the response (see Supplementary Figure S3). Voltage amplifier offset is adjusted by comparing the response of the bolometer at equilibrium with its calibration curve and subtracting the difference.

System modelling

The theoretical curves were obtained by calculating the current and power arising from the solution of a Markovian classical master equation on the island excess charge n [2]

$$\frac{d}{dt}p\left(n,t\right)=\sum_{n\neq n'}\gamma_{n'n}p\left(n',t\right)-\gamma_{nn'}p\left(n,t\right). \tag{3}$$

Here $p\left(n,t\right)$ is the probability of the island to have n excess charges at time t and $\gamma_{nn'}$ is the total transition rate from the state n to n' which is directly related to the tunnelling rates through a NIS interface. The equation is solved in the steady state ($dp\left(n,t\right)/dt=0$) for the DC regime and with periodic conditions ($p\left(n,0\right)=p\left(n,\tau\right)$, with $\tau=1/f$) for the turnstile operation. The current through the left junction (L) is related to the occupation probabilities through

$$\begin{aligned}I_{\mathrm{L}}=e\sum_{n}p\left(n\right)\left(\Gamma^{\mathrm{L}}_{n\to n+1}-\Gamma^{\mathrm{L}}_{n\to n-1}\right)\\+2e\sum_{n}p\left(n\right)\left(\Gamma^{\mathrm{L}}_{n\to n+2}-\Gamma^{\mathrm{L}}_{n\to n-2}\right),\end{aligned} \tag{4}$$

where $\Gamma^{\mathrm{L}}_{n\to n\pm1}$ denotes the single-electron elemental process rates and $\Gamma^{\mathrm{L}}_{n\to n\pm2}$ second order Andreev process rates. The current can be averaged along one cycle as $\langle I_{\mathrm{L}}\rangle=1/\tau\int_0^\tau dtI_{\mathrm{L}}$.

The power injected to the transistor leads by stationary elementary events $\dot{Q}^{\mathrm{R/L,S}}_{n\to n\pm1}$ gives the average injected power during one driving cycle as

$$\left\langle P_{\mathrm{R/L}}\right\rangle=\frac{1}{\tau}\int_0^\tau dt\sum_{n}p\left(n\right)\left(\dot{Q}^{\mathrm{S,R/L}}_{n\to n+1}+\dot{Q}^{\mathrm{S,R/L}}_{n\to n-1}\right). \tag{5}$$

In contrast to the current, the individual elementary tunnelling events contribute always additively to the power. For the DC case and for calculating the instantaneous power the integral is omitted. For obtaining accurate results comparable to experiments and because of the stiffness of the time periodic problem, an alternative numerical solution to Eq. (3) based on propagation of the probability was carried out (see Supplementary Section S4). For further understanding of the instantaneous behaviour of the quantities, Eq. (3) was also solved at discrete cycle intervals using a variable order method.

DATA AVAILABILITY

Data supporting the manuscript and supplementary Figures as well as further findings are available at `https://doi.org/10.5281/zenodo.5727157` [3].

CODE AVAILABILITY

The codes for generating the measured manuscript and supplementary Figures are available at `https://doi.org/10.5281/zenodo.5727157` [3]. Algorithms for generating calculated curves are available from the corresponding author upon reasonable request.

* marco.marinsuarez@aalto.fi

[1] Meschke, M., Kemppinen, A. & Pekola, J. P. Accurate coulomb blockade thermometry up to 60 kelvin *Phil. Trans. R. Soc. A* **374**, 20150052 (2016).
[2] Marín-Suárez, M., Peltonen, J. T. & Pekola, J. P. Active quasiparticle suppression in a non-equilibrium superconductor. *Nano Lett.* **20**, 5065–5071 (2020).
[3] Marín-Suárez, M., Peltonen, J. T., Golubev, D. S. & Pekola, J. P. Data for Frequency to power conversion by an electron turnstile. *Zenodo.* `10.5281/zenodo.5727157` (2021).

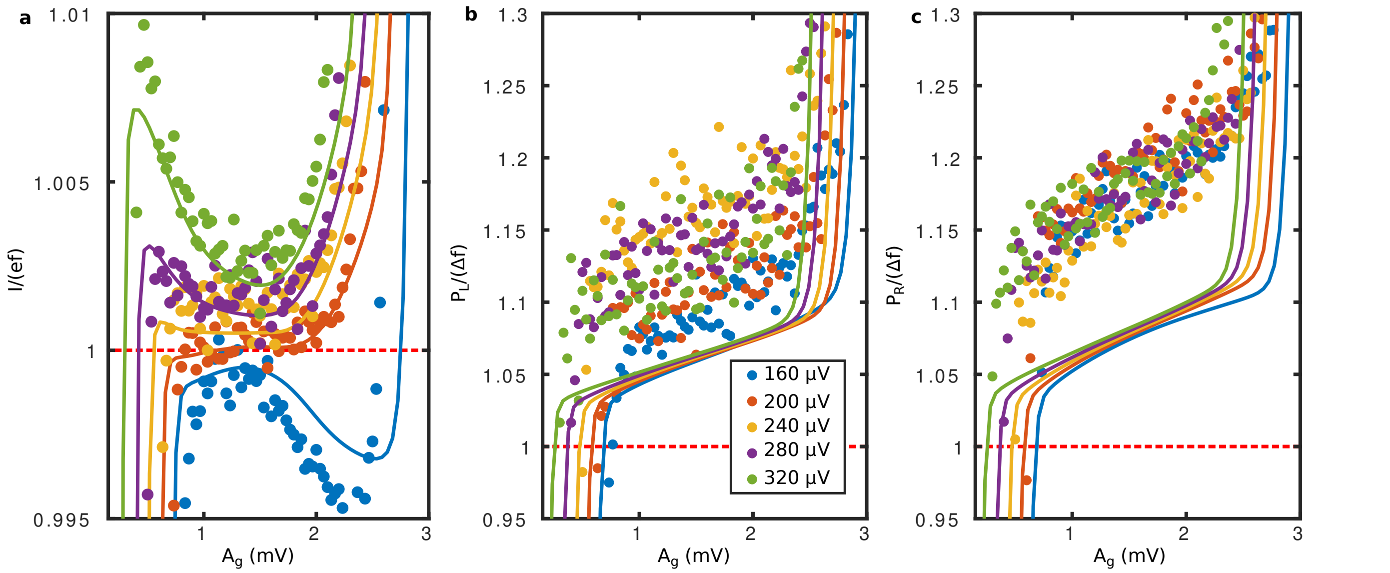

Extended Data FIG. 1. **Current and injected power at $f = 20\,\mathrm{MHz}$.** Extension of Fig. 4a. (a) Measured (dots) and simulated (lines) pumped current, colors correspond to the legend of panel (b). Data for $V_\mathrm{b} = 240\,\mu\mathrm{V}$ has been included for completeness. (b) As in (a) for the power injected to the left lead. (c) As in (b) for the right lead.

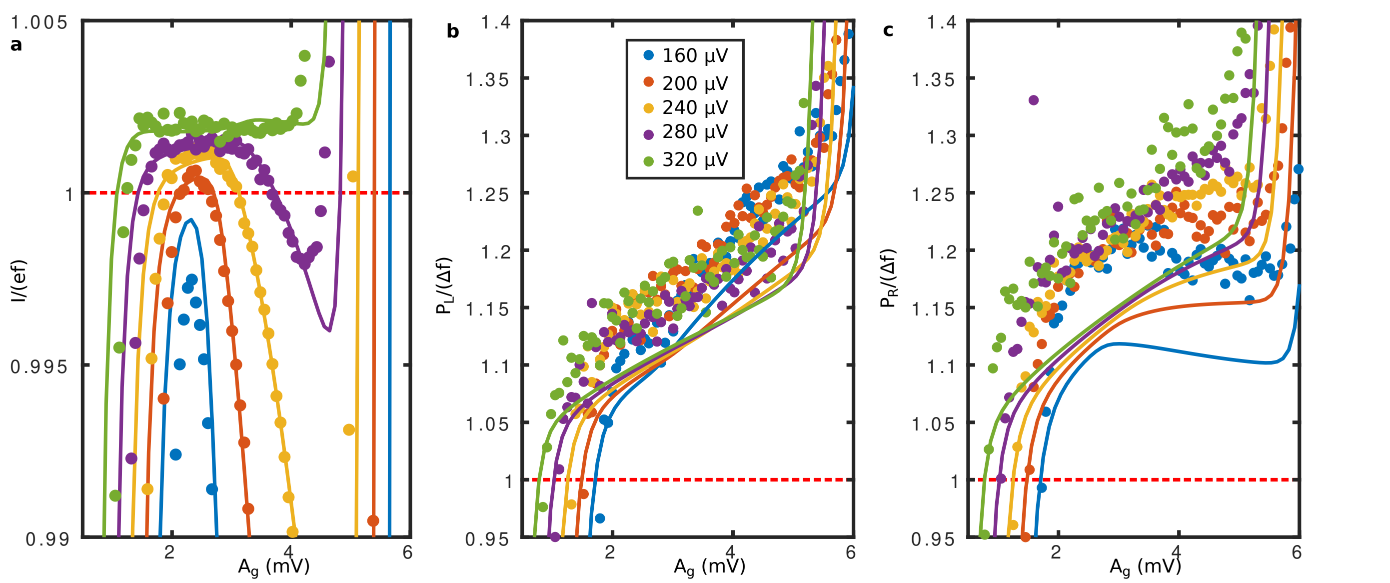

Extended Data FIG. 2. **Current and injected power at $f = 60\,\mathrm{MHz}$.** Extension of Fig. 4b. (a) Measured (dots) and simulated (lines) pumped current, colors correspond to the legend of panel (b). Data for $V_\mathrm{b} = 160\,\mu\mathrm{V}$ has been included for completeness. (b) As in (a) for the power injected to the left lead. (c) As in (b) for the right lead. Observe how power is more equally distributed as back-tunnelling disappears at $V_\mathrm{b} = 320\,\mu\mathrm{V}$. This makes the power transmitted through the most transparent junction to decrease with bias voltage.

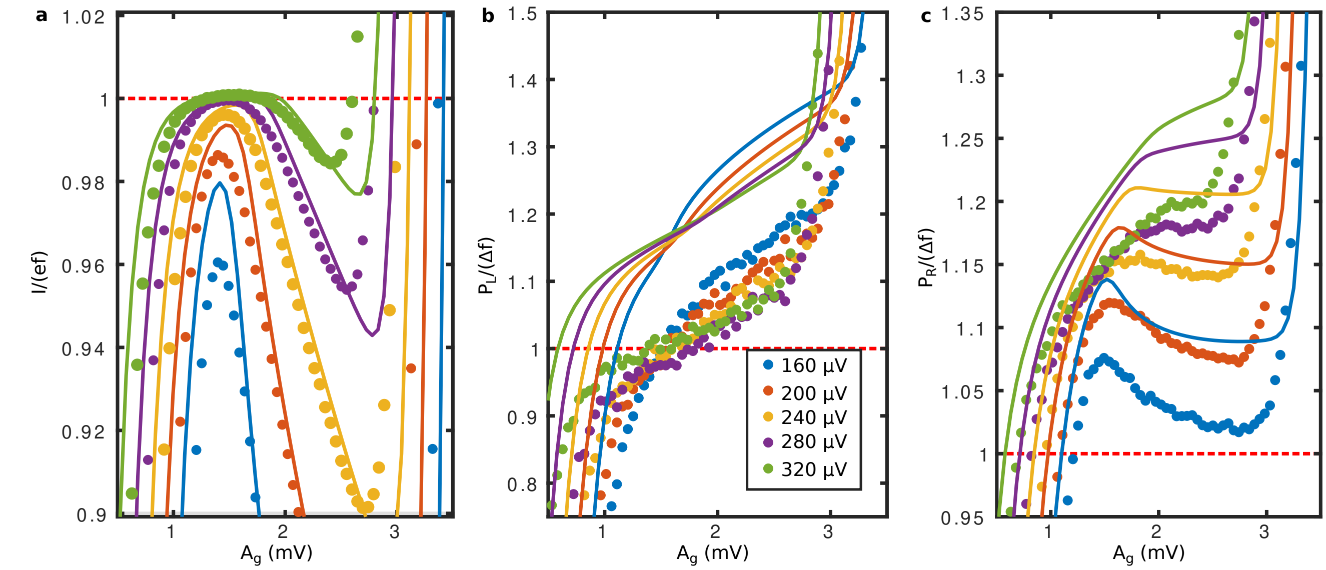

Extended Data FIG. 3. **Current and injected power at** $f = 120\,\mathrm{MHz}$**.** (a) Measured (dots) and simulated (lines) pumped current, colors correspond to the legend of panel (b). (b) As in (a) for the power injected to the left lead. (c) As in (b) for the right lead. Here the higher base temperature has decreased the bolometers trapping efficiencies and hence the experimental power curves appear systematically below the calculated ones. However, the amount of injected power through the transistor junctions is not expected to vary. Observe how power is more equally distributed as back-tunnelling reduces. This makes the power transmitted through the most transparent junction to decrease with bias voltage.

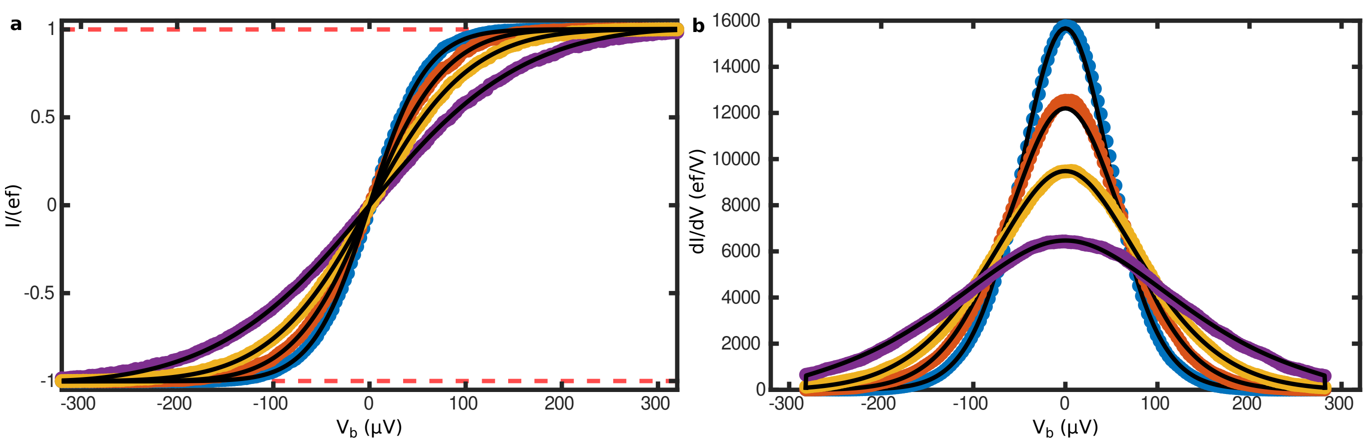

Extended Data FIG. 4. **Pumped current against bias voltage.** (a) Experimental pumped current at constant amplitude with a driving frequency of 30, 60, 80, 160 MHz as blue, red, yellow and purple dots, respectively. Black lines are calculations made with a Markovian equation, the dashed lines designate the ideal pumped current $I = ef$. (b) Differential conductance obtained by numerical differentiation of panel (a) data. Black lines are numerical derivatives of calculations of panel (a). Lower operation frequencies give sharper pumped current and conductance.